

Monte Carlo Simulation of X-ray Transport

John Meneghini^{a)}

Department of Physics, Saint Vincent College, Latrobe, PA 15650

^{a)}Corresponding author: john.meneghini@stvincent.edu

Abstract. An article usually includes an abstract, a concise summary of the work covered at length in the main body of the article. It is used for secondary publications and for information retrieval purposes.

INTRODUCTION

TRANSPORT THEORY

In order to represent the computational domain discretely, space is broken up into a grid of voxels (a pixel with volume), with each voxel being assigned a particular material ID depending on the geometries and compounds/elements in the domain. With our discrete space, given a photon position \vec{r} , the corresponding voxel in which the photon resides can be calculated. Therefore, a particular material can be associated with all possible \vec{r} 's in the domain.

A photon's position in space after taking the n -th step in the domain \vec{r}_n is represented by the following parametric ray equation:

$$\vec{r}_n = \vec{r}_{n-1} + \hat{d}t_n, \quad (1)$$

where \vec{r}_{n-1} is the initial position before the n -th step, \hat{d} is a unit vector in the direction of the step, and t_n is the distance of the n -th step.

In order to sample t_n , we utilize the following probability distribution function (PDF) $p(t)$ of the distance traveled t by a photon of energy E through material M before interacting:

$$p(t) = n\sigma \exp[-t(n\sigma)], \quad (2)$$

where n is the number density of M and $\sigma = \sigma(E, M)$ is the microscopic cross-section of M at E .

Using the inversion method for sampling a PDF, it follows that random values of the free path t can be generated with the following equation:

$$t = -\frac{1}{n\sigma} \ln \gamma, \quad (3)$$

where γ is a uniformly distributed random number in the interval $(0, 1)$. This value of t is sampled for each step and is used as t_n in Eq 1 to determine the length of the n -th step.

SURFACE AND DELTA-TRACKING

If, after taking a step, the photon lands in a voxel with a different material, then the corresponding free path for the new material to be accounted for. This method, called surface-tracking, requires photons to be stopped at voxel boundaries and intersections with surrounding voxels to be calculated, which can be computationally intensive for materials that have a large average free path.

Alternatively, the delta-tracking algorithm offers a solution by sampling the maximum cross-section σ_{\max} in the computational domain. This, in turn, brings down the average free path to the minimum in the domain. To account for this decrease in free path, the algorithm introduces delta interactions as an alternative to real interactions, resulting in no change to the energy or direction. The probability of delta interaction P_δ is given by the following equation:

$$P_\delta = \frac{\sigma_{\max}(E) - \sigma(E, M)}{\sigma_{\max}(E)}, \quad (4)$$

where E is the energy of the photon undergoing the step, and M is the material corresponding to the position of the photon at the end of the step. Note that when the photon lands in the material corresponding to the maximum cross-section, $\sigma(E, M) = \sigma_{\max}$ and $P_\delta = 0$. On the contrary, if the photon landed in air and the domain's maximum cross-section corresponded to lead, then $\sigma(E, M) \ll \sigma_{\max}$, making $P_\sigma \approx 1$.

Overall, delta-tracking is significantly more computationally efficient for domains with similar cross-sections and can be shown to yield equivalent results to surface-tracking.

PHOTON INTERACTIONS

If a delta interaction does not occur, then a real interaction is sampled. Therefore, the probability of a real interaction P_r is directly related to P_δ by

$$P_r = 1 - P_\delta, \quad (5)$$

where P_δ is given by Eq. 4.

If a real interaction occurs in material M , then probability of interaction i occurring is

$$P_i = \frac{\sigma_i(E, M)}{\sigma(E, M)}, \quad (6)$$

where σ_i is the cross-section of interaction i .

If there are N possible interactions for a particular E and M , then $\sigma(E, M)$ is calculated as so

$$\sigma(E, M) = \sum_{i=1}^N \sigma_i(E, M). \quad (7)$$

For x-rays, there are three possible photon interactions:

1. Photoelectric Effect

In the photoelectric effect model used in MIDSX, a rather simple approach is taken. When a photon interacts with an atom's electron, the photon is terminated and all energy is deposited at the location of interaction. In general purpose particle transport code systems, when a photoelectric interaction occurs, a photon of energy E is absorbed by an electron in subshell i , causing the electron to leave the atom with energy $E_e = E - U_i$, where U_i is the binding energy of the i th subshell. In addition, photons are emitted due to atomic relaxations. For photon energies in the medical imaging range (30 - 120 keV), the energy of the released electrons does not allow for significant traversal through typically used materials, such as tissue, bone, and fat. This limited traversal results in a localized dose distribution, in turn, validating the model used by MIDSX.

2. Coherent Scattering

Thomson scattering is defined as an incoming photon of energy E elastically scattering with a free electron at rest, resulting in a scattered photon of same energy E . The atomic DCS per unit solid angle Ω for the interaction can be derived with classical electrodynamics, and is given by

$$\frac{d\sigma_T}{d\Omega} = r_e^2 \frac{1 + \cos^2(\theta)}{2}, \quad (8)$$

where r_e^2 is the classical electron radius.

In an atom, photons scatter off bound electrons rather than the free electrons described by Thomson scattering, resulting in what is known as coherent (Rayleigh) scattering at . The DCS per unit solid angle Ω of the interaction, ignoring absorption edge effects, is given by

$$\frac{d\sigma_{Co}}{d\Omega} = \frac{d\sigma_T}{d\Omega} F(x, Z), \quad (9)$$

where x is the momentum transfer between the photon and atom, Z is the atomic number of the atom, and $F(x, Z)$ is the atomic form factor. x is related to the scattering angle θ by

$$x = ak\sqrt{1 - \cos \theta}, \quad (10)$$

where

$$a = \frac{m_e c^2}{\sqrt{2}hc} \quad \text{and} \quad k = \frac{E}{m_e c^2}, \quad (11)$$

where m_e is the mass of an electron, c is the speed of light, and h is Planck's constant.

The DCS per unit solid angle Ω can be integrated over ϕ to obtain the DCS per unit polar angle θ :

$$\frac{d\sigma_{Co}}{d\theta} = \pi r_e^2 \sin \theta (1 + \cos^2 \theta) F(x, Z)^2. \quad (12)$$

The PDF of the polar angle θ is then given by

$$p(\theta)d\theta = \frac{d\sigma_{Co}}{d\theta} \frac{1}{\sigma_{Co}} d\theta = \frac{\pi r_e^2}{\sigma_{Co}} \sin \theta (1 + \cos^2 \theta) F(x, Z)^2 d\theta. \quad (13)$$

The PDF of θ can be transformed into a PDF of $\mu = \cos \theta$, resulting in

$$p(\mu) = \frac{\pi r_e^2}{\sigma_{Co}} (1 + \mu^2) F(x, Z)^2. \quad (14)$$

To then sample μ for a particular scattering event, the inversion method is used. In particular, a look up table for the CDF of $P(\mu)$ is generated for each material in the domain for a grid of μ values. The details of this algorithm are discussed in Appendix ...

3. Incoherent Scattering

Incoherent (Compton) scattering is defined as an incoming photon of energy E interacting with an atom's electron, resulting in a scattered photon of energy E' and an released electron with energy $E_e = E - E' - U_i$, where U_i is the binding energy of the interacting subshell. While coherent scattering effectively interacts with atom itself, incoherent scattering interacts with the electron. The DCS per unit solid angle Ω of the interaction was derived by Klein and Nishina in 1929, making it one of the first findings of quantum electrodynamics. The Klein-Nishina formula is given by

$$\frac{d\sigma_{KN}}{d\Omega} = \frac{r_e^2}{2} \left(\frac{E'}{E} \right)^2 \left(\frac{E'}{E} + \frac{E}{E'} - \sin^2 \theta \right), \quad (15)$$

Note that when $E' = E$, the KN DCS is equal to the Thomson DCS, showing that incoherent scattering is a generalization of coherent scattering for inelastic interactions.

Applying conservation of energy and momentum to free electron at rest, the following equation can be derived relating the scattered photon energy E' to the scattering angle θ and the incident photon energy E :

$$E' = \frac{E}{1 + k(1 - \cos \theta)}. \quad (16)$$

Similar to the Thomson DCS, the KN DCS assumes a free electron at rest. In an atom, the electron is bound, resulting in a modified DCS. In the case of incoherent scattering, the KN DCS is modified by the Coherent Scattering Function, making the DCS per unit solid angle Ω of the interaction

$$\frac{d\sigma_{In}}{d\Omega} = \frac{d\sigma_{KN}}{d\Omega} S(x, Z). \quad (17)$$

Instead of directly sampling the PDF of the DCS, μ is first sampled using the acceptance-rejection method developed by Ozmutlu, then $S(x, Z)$ is sampled once again with the acceptance-rejection method. The details of this algorithm are discussed in Appendix ...

METHODS

In order to simulate the transport of x-rays through a domain, the following is required:

1. The geometry of the domain
2. The materials in the domain
3. The associated cross-sections, form factors, and scattering functions of the materials
4. The source of the x-rays (energy spectrum, position, and direction)
5. The number of photons to simulate

and to retrieve information about the performed simulation, the following is required:

1. Geometries to check for intersection
2. Quantities to tally
3. Derived quantities to calculate from tallied quantities

GEOMETRY

In MIDSX, the geometry of the domain is represented by a 3D array of voxels, with each voxel being assigned a material ID. The domain is assigned a particular size, indicated by its spatial extent along the x, y, and z dimensions. In addition, the domain is assigned a background material ID. Geometries inside the domain are specified by NIFTI files [1]. These NIFTI files are assigned material IDs, spatial size, voxel size, and an origin, which is the location of the voxel in the domain that corresponds to the origin of the NIFTI file. After constructing the NIFTI files, the domain is defined by supplying the background material ID, domain size, and a list of NIFTI files into a custom .domain file, which is then read by the MIDSX executable.

In the code, both a `VoxelGrid` and `ComputationalDomain` object are created, with the `ComputationalDomain` consisting of the specified dimensions, background material ID, and a vector of `VoxelGrid` objects which are created via the provided NIFTI files. Do determine the current material of a photon, it is first determined if the photon is inside the `ComputationalDomain`. If so, it then checks if the photon is inside any of the `VoxelGrid` objects. If so, it is then determined which `Voxel` the photon is located inside the `Voxel`, then the corresponding material ID is returned. If the photon is not inside the `ComputationalDomain`, then the photon is terminated.

MATERIALS & DATA

In order to simulate the transport of x-rays through a domain, the materials in the domain must be specified. In MIDSX, materials are all defined in an SQLite database [3], which is read by the MIDSX executable. The database contains the following information for each element:

1. Symbol
2. Atomic Number
3. Mass
4. Mass Density
5. Number Density
6. Mass Number

All of the above data was obtained from the `periodictable` [6] and `mendelev` [7] python packages. In addition, the database contains the following data from the EPDL database [2] for each element:

1. Total Microscopic Cross-Section
2. Photoelectric Microscopic Cross-Section
3. Coherent Scattering Microscopic Cross-Section
4. Incoherent Scattering Microscopic Cross-Section
5. Atomic Form Factor
6. Scattering Function

In MIDSX, all the above data is initialized upon creation of the `InteractionData` object with a vector of strings of materials names. These material names correspond to entries in the SQLite database, which contains a table of material compositions and mass densities which were obtained from NIST's mass attenuation coefficient database [4]. The `InteractionData` object contains a map of `Material` objects with their names, along with additional computed data, such as the maximum cross-section which is used for delta-tracking. The `Material` objects construct the above data for the specified material by performing an additivity approximation of the data for each element in the material as described by [5]. The data is separated into two further objects: `MaterialData` and `MaterialProperties`. `MaterialData` contains the microscopic cross-sections, form factors, and scattering functions, while `MaterialProperties` contains the mass density, number density, and mass.

In addition to retrieving and storing the above data, the `MaterialData` object constructs interpolators for all its data. The interpolators for each type of data vary depending on its shape. For example, the photoelectric and total cross-sections are interpolated with a log-log linear interpolator, while the incoherent and coherent cross-sections are interpolated with a log-log cubic spline interpolator.

Source

To generate the initial position, direction, and energy of a photon, a `PhotonSource` object is initialized with a `SourceGeometry`, `Directionality`, and an `EnergySpectrum` object. The three initializing object are virtual classes, allowing the user to specify the attributes of the source. The inheritance structure is shown in Fig ().

Tallies

To measure simulation data, one must first decide when to trigger the measurement. In particular, MIDSX supports both surface and volume geometries that trigger when a photon passes through or enters the geometry, respectfully. For surfaces, users can choose discs and rectangles, while for volumes, there are only cuboids at the moment.

At the start of the simulations, users can specify quantities that they want measured upon the trigger of a specific geometry. For surfaces, these include incident photon energy, entrance cosine, and number of photons, while for volumes, in addition to their own implementation of incident energy and number of photons, the quantities energy deposition and number of interactions are available for measurement. Furthermore, each quantity has the ability to specify between photons that underwent a single coherent scatter, a single incoherent scatter, multiple scatters, and no scatters. While this does noticeably increase the computation time, it was necessary to validate the interaction models used in MIDSX.

At the end of simulation, one might want to calculate additional derived quantities from the tallied quantities from the simulation. With this mind, MIDSX contains a `DerivedQuantity` object that can calculate planar fluence and air kerma, which were implemented for half value layer experiments.

Using the described theory and methodology, the object `PhysicsEngine` transports a photon through the computational domain until termination. This process is described in Figure 1.

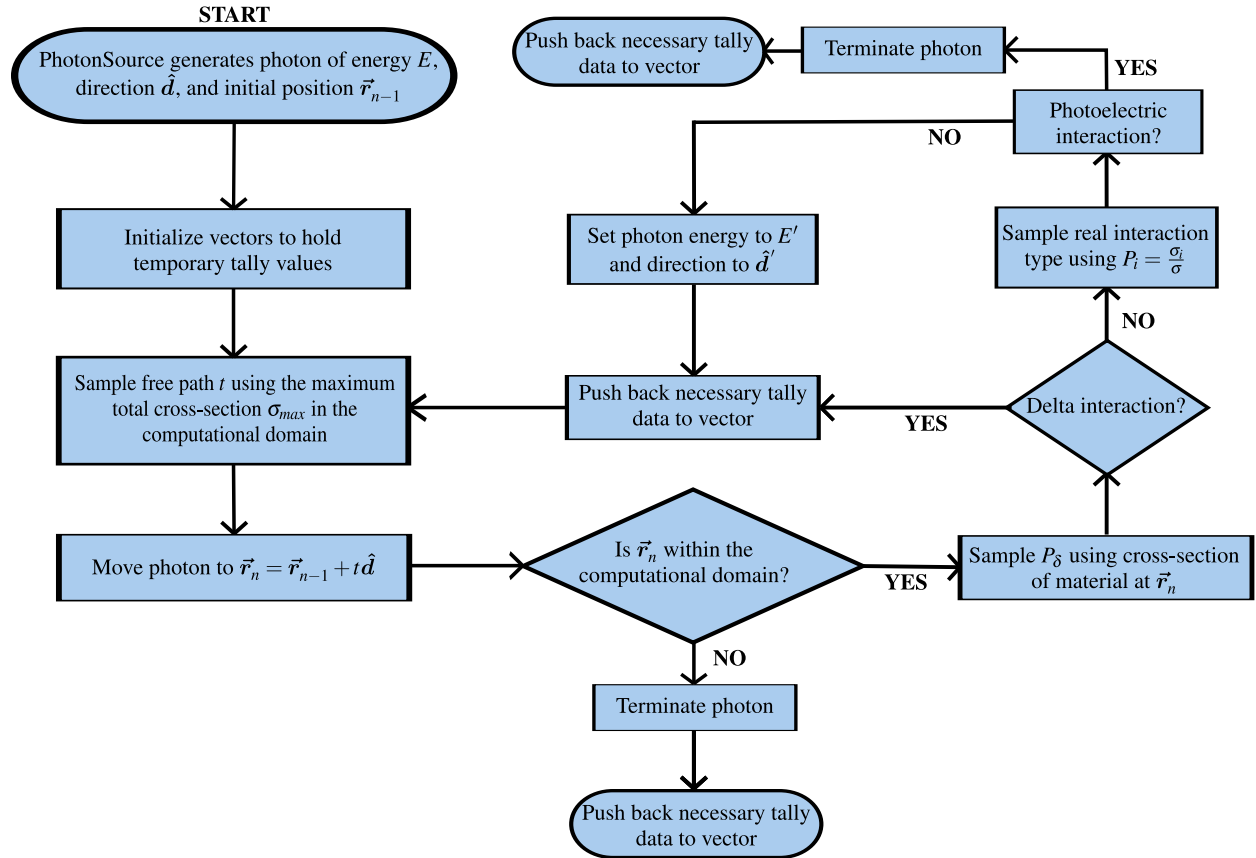


FIGURE 1. Diagram of GE MiniView 6800 Mini C-Arm used in effective energy measurements.

RESULTS

In order to validate the accuracy of MIDSX, validation simulations were performed and compared to reference data obtained by American Association of Physicists in Medicine Task Group Report 195 (TG-195) [8]. The simulations performed from TG-195 were Case 1: "Half Value Layer", Case 2: "Radiography and Body Tomosynthesis", and Case 5: "CT with a Voxelized Solid". For Case 1, the primary air kerma was measured on a far away, circular region of interest (ROI) with a cone beam collimated such that all primary particles would be incident upon the ROI. The primary air kerma was measured with the domain filled only with air, and then compared to the measured air kerma with an Al filter of specified thickness placed between the source and ROI. By setting this thickness to correspond the half value layer (HVL) and quarter value layer (QVL) for a particular spectrum, one is able to validate the material attenuation properties of an MC code system. The ratios of the primary half value layer (HVL) and air kermas to the primary background air kermas is represented by R_1 and R_2 , respectively. The simulation was performed for the monoenergetic energies 30 keV and 100 keV, along with the polyenergetic spectrums of 30 kVp and 100 kVp, which were provided by TG-195. MIDSX's results for Case 1 agree to within 0.32% of the mean results published by TG-195, and only the simulation results of 100 keV x-ray spectrum fell withing the range of the published results for both the HVL and QVL simulations. The results of Case 1 are presented in Fig 2.

For Case 2, a full-field and pencil beam x-ray source were directed towards a rectangular tissue phantom at 0° and 15° with respect to the z-axis. Directly behind and inside the phantom, a grid of square ROIs and cube VOIs were placed, respectively. The simulation was performed for the TG-195 provided polyenergetic spectrum of 120 kVp and its mean energy of 56.4 keV. For the 0° full-field ROI measurements not shown in this paper due page constraints, a $< 3\%$ mean percent error (MPE) is seen for MIDSX's results to each ROI simulation. Furthermore, for the 0° pencil-beam ROI measurements shown in Fig 4, a $< 2.1\%$ MPE is observed for each ROI simulation expect for the case of a single incoherent scatter. In this particular case, MIDSX's results for ROI 4 and 5 are significantly lower, with the MPE reaching 10% for ROI 5. In the full-field VOI energy deposition measurements depicted in Fig 3, the disagreement between code systems is varied with an MPE of less than 0.1% for the 0° source. Conversely, for the MIDSX results at 15° , the MPE reaches an unexpectedly larger value of approximately 0.5%.

For Case 5, a fan beam was collimated to the center of a voxelized human torso phantom provided by TG-195. In order to replicate a CT image, the simulation was repeated for several angles along a circle surrounding the phantom. The simulation was performed with Case 2's 120 kVp energy spectrum, and energy deposition was measured in the different materials/organs composing the phantom. Almost all of MIDSX's results for the 0° source presented in Fig 5 are systematically lower than the mean of the reference code systems, with MPE's ranging from 1.1% to 6.3%. This pattern is disrupted by the thyroid, which is larger than the mean by 2.9%. In order to quantify the cumulative error, the root mean square percent error (RMSPE) was calculated using each organ result, which resulted in the RMSPE for MIDSX being 5%.

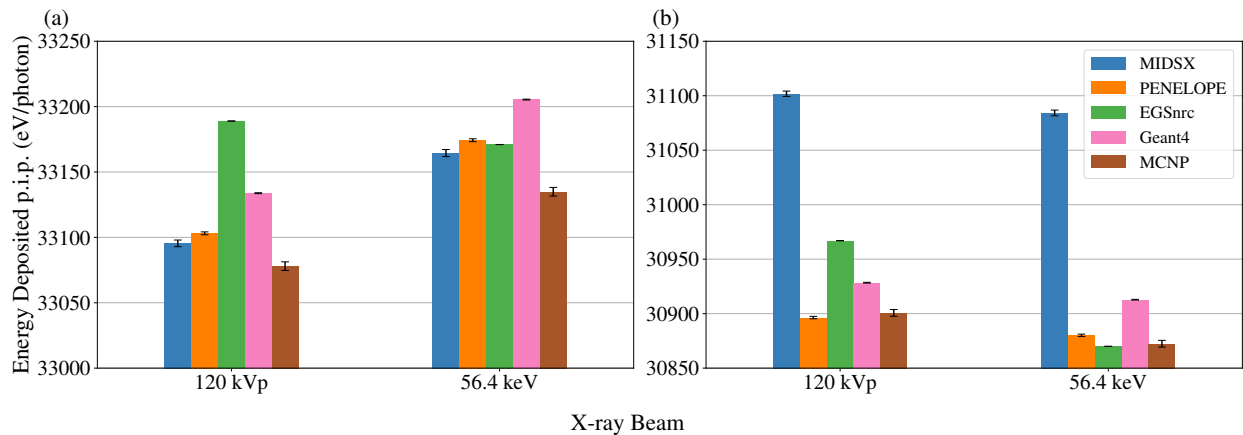


FIGURE 3. The energy deposited per initial photon (eV/photon) in the simulated tissue for the full-field simulation as described by Case 2. The simulation was performed at 56.4 keV and 120 kVp at both (a) 0° and (b) 15° , with the 120 kVp spectrum provided by TG-195.

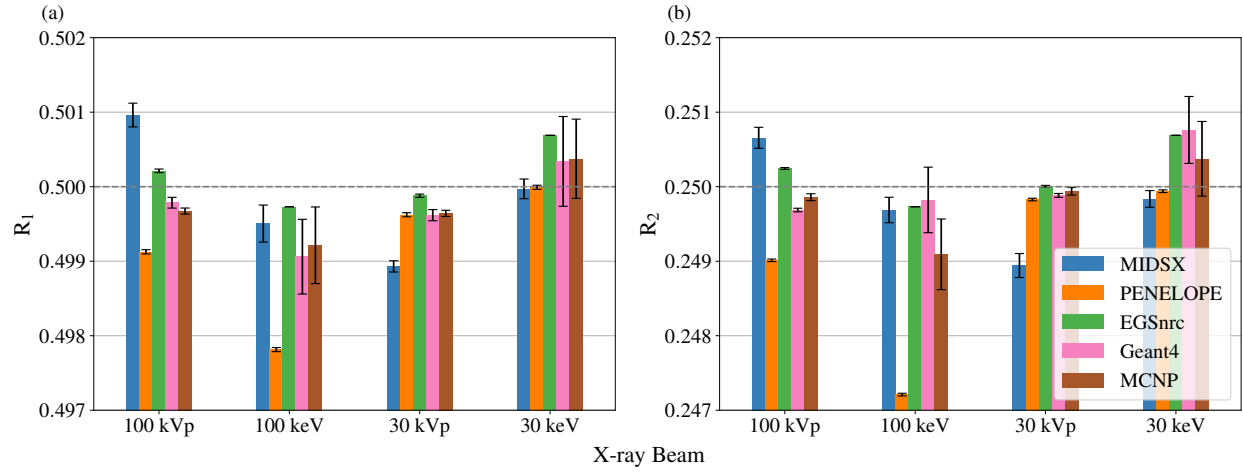


FIGURE 2. Results for the (a) HVL and (b) QVL simulations as described by Case 1. The ratios of the primary HVL and QVL air kermas to the primary background air kermas is represented by R_1 and R_2 , respectively. The simulation was performed for the monoenergetic energies 30 keV and 100 keV, along with the polyenergetic spectra of 30 kVp and 100 kVp, which were provided by TG-195.

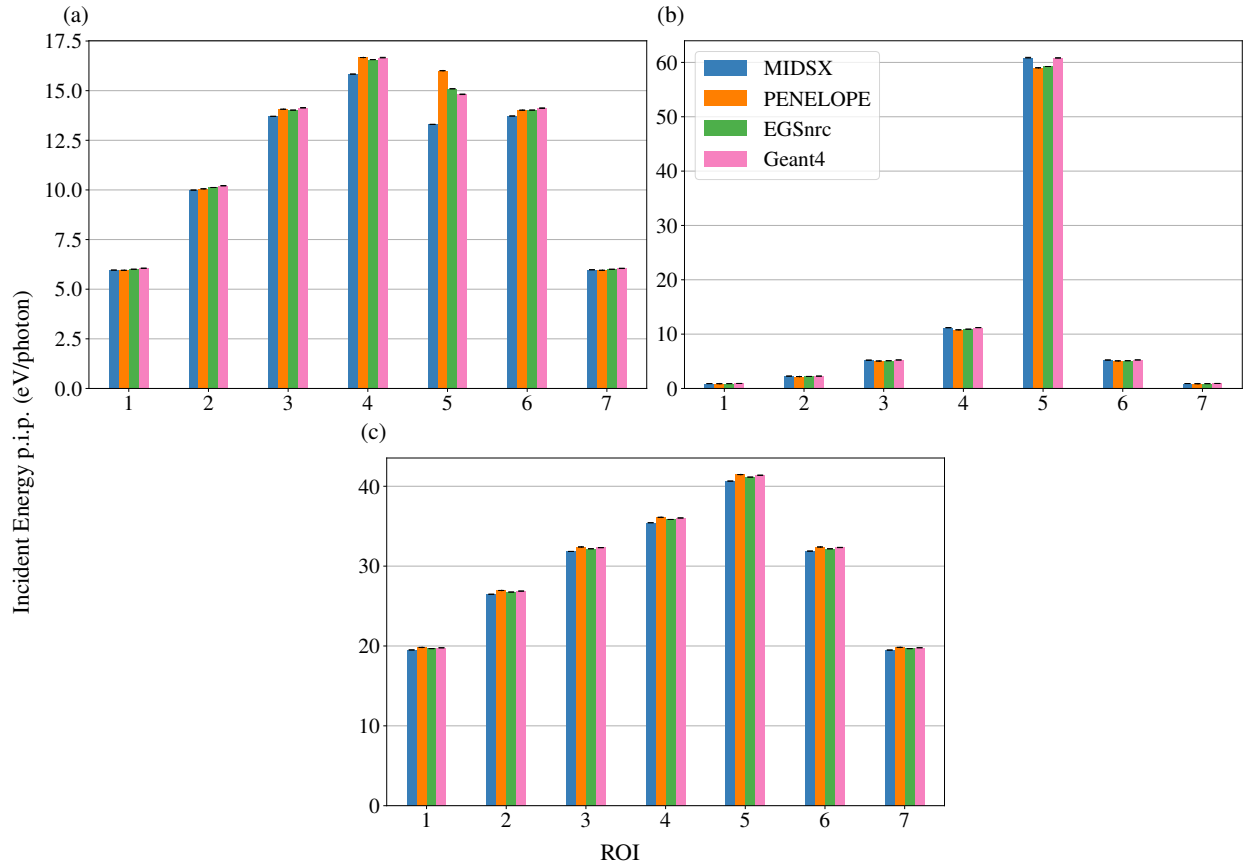


FIGURE 4. The energy per initial photon (eV/photon) of photons incident upon each region of interest (ROI) for the 0° , pencil beam, 56.4 keV simulation as described by Case 2. The incident energy was determined separately for photons that underwent (a) a single incoherent scatter, (b) a single coherent scatter, (c) and multiple scatters.

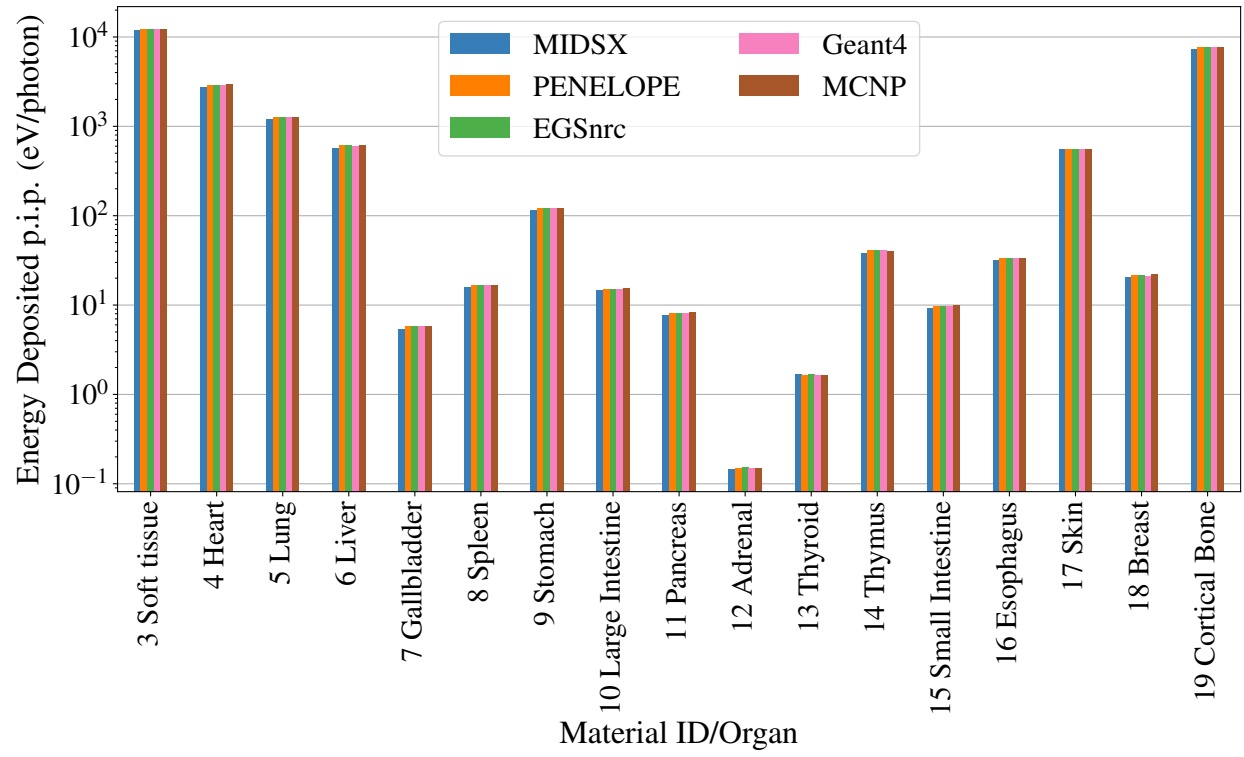


FIGURE 5. The energy deposited per initial photon (eV/photon) in the material IDs for the 0° , 120 kVp simulation as described by Case 5.

DISCUSSION

Overall, MIDSX shows varied but reasonable agreement with the reference codes systems of TG-195. For Case 1, excellent agreement is observed, in effect validating the total and max cross-section data used in δ tracking, and the sampling of a discrete x-ray energy spectrum. This makes MIDSX a reliable and accurate option for primary particle measurements.

For the ROIs of Case 2, agreement is seen almost universally, except for the single incoherent scatter deposition energy in ROI 4 and 5 for the pencil beam source shown in Fig 4. In particular, the results reached a max MPE of 10% for ROI 5, indicating an error in the incoherent scattering energy/angular distribution sampling algorithm. This discrepancy is likely a result of an error in the rejection sampling algorithm employed by MIDSX. While this algorithm shows agreement for the full-field ROI 5, the geometry of the ROI, combined with the pencil beam, results in only narrow angle scatters hitting the ROI. Since the scattering angle distribution of incoherent scattering at the medical imaging energy range contains a vertical asymptote approaching 0 at scattering angle $\theta = 0^\circ$, there is likely some form of numerical instability presenting itself in the algorithm that needs to be analyzed. In addition, the 15° full-field tissue energy deposition measurements were larger than the reference code systems', with an MPE of 0.5%. With the MPE increasing significantly from the 0° to 15° measurements, this hints at a possible geometric error with source and/or body. However, the source's position and angular distribution, along with domain's and tissue's dimensions very extensively verified, making the geometry of the scene less likely to be the source of the discrepancy.

For Case 5, almost all organ energy deposition results were lower than the reference code results, with the MPE % reaching 6.3%. An exception was seen with the thyroid, which had the uniquely larger energy deposition result with an MPE of 2.9%. One common error reported by TG-195 that could result in the observed discrepancies is the incorrect orientation of the voxelized phantom in the computational domain. On top of checking the scenes geometry and the .domain file, the orientation was verified by taking the RMSPE of the MIDSX data with respect to the results of each simulated angle reported by TG-195. As expected, the RMSPE with respect the 0° was the minimum, further solidifying the belief that the phantom's orientation during the CT simulation is accurate.

However, despite the orientation being verified, the deviation of MIDSX energy deposition results for both Case 2 and 5 raises concerns. This suggests that there may be other underlying issues or intricacies in the MIDSX system that need further investigation. Potential factors could include the software's handling of certain physics processes, voxel resolution, or computational approximations. It's imperative for future research to delve deeper into these aspects to pinpoint and rectify the source of the systematic errors observed in the MIDSX results.

ACKNOWLEDGMENTS

We wish to acknowledge the support of the author community in using REVTeX, offering suggestions and encouragement, testing new versions,

REFERENCES

1. R.W. Cox, John Ashburner, Hester Breman, Kate Fissell, C. Haselgrove, C.J. Holmes, J.L. Lancaster, D.E. Rex, S.M. Smith, J.B. Woodward, and Stephen Strother. A (sort of) new image data format standard: Nifti-1. volume 22, 01 2004.
2. Dermott E Cullen. A Survey of Photon Cross Section Data for use in EPICS2017. November 2017.
3. Richard D Hipp. SQLite, 2020. URL <https://www.sqlite.org/index.html>.
4. J. H. Hubbell and S. M. Seltzer. X-Ray Mass Attenuation Coefficients, 2004.
5. Esam M.A. Hussein. Chapter three - cross sections. In Esam M.A. Hussein, editor, *Radiation Mechanics*, pages 153–245. Elsevier Science Ltd, Oxford, 2007. ISBN 978-0-08-045053-7. doi:<https://doi.org/10.1016/B978-008045053-7/50004-5>. URL <https://www.sciencedirect.com/science/article/pii/B9780080450537500045>.
6. Paul Kienzle. periodictable - a python library for periodic table of the elements, May 2022. URL <https://github.com/pkienzle/periodictable>.
7. Łukasz Mentel. mendeleev - a python package with properties of chemical elements, ions, isotopes and methods to manipulate and visualize periodic table., March 2021. URL <https://github.com/lmentel/mendeleev>.
8. Ioannis Sechopoulos, Elsayed S. M. Ali, Andreu Badal, Aldo Badano, John M. Boone, Iacovos S. Kyprianou, Ernesto Mainegra-Hing, Kyle L. McMillan, Michael F. McNitt-Gray, D. W. O. Rogers, Ehsan Samei, and Adam C. Turner. Monte Carlo reference data sets for imaging research: Executive summary of the report of AAPM Research Committee Task Group 195. *Medical Physics*, 42(10):5679–5691, October 2015. ISSN 0094-2405, 2473-4209. doi:10.1118/1.4928676. URL <https://onlinelibrary.wiley.com/doi/10.1118/1.4928676>.